

Recurrent solutions of Alber's equation for random water-wave fields

M. STIASSNIE, A. REGEV AND Y. AGNON

Faculty of Civil & Environmental Engineering, Technion, Haifa 32000, Israel
miky@tx.technion.ac.il

(Received 9 November 2006 and in revised form 4 November 2007)

The study addresses the linear instability of narrow spectra homogeneous seas and its subsequent evolution in time, subject to inhomogeneous disturbances. Specifically, we study unidirectional spectra, where according to the kinetic equation no spectral evolution is expected. In the region of instability, recurrent evolution is discovered. This recurrence is the stochastic counterpart of the Fermi–Pasta–Ulam recurrence obtained for the cubic Schrödinger equation.

1. Introduction

The nonlinear evolution in time (t) and space (x) of ocean-wave fields is usually described by equations for the free-surface elevation $\eta(x, t)$, or related quantities, such as an amplitude spectrum given by its x to k Fourier transform. For deep water, two frequently mentioned deterministic equations are: Zakharov's equation for broad-amplitude spectra and the cubic Schrödinger equation for narrow spectra (see Zakharov 1968).

Randomness is introduced through the concept of ensemble averaging. The ensemble average is defined as an average taken over randomly chosen initial phases allocated to the various modes of a continuous spectrum, and is denoted by angle brackets $\langle \cdot \rangle$. Since $\langle \eta \rangle = 0$, the next variable of interest is:

$$c(x, r, t) \equiv \langle \eta(x + \frac{1}{2}r, t) \eta(x - \frac{1}{2}r, t) \rangle. \quad (1.1)$$

A wave field is called homogeneous if the above two-point correlation c , with spacing r , is independent of x , i.e. $c = c(r, t)$.

The most frequently used stochastic model, is Hasselmann's (1962) kinetic equation. The kinetic equation (and also Janssen's (2003) non-resonant kinetic equation, as well as Annenkov & Shrira (2006) extended kinetic equation), were derived for homogeneous wave fields, and are written in terms of the r to k Fourier transform of $c(r, t)$, i.e. in terms of the energy spectrum $S(k, t)$. A key step in the derivation of the kinetic equation is the assumption that the phases of the components, however close to each other in k space, remain uncorrelated to lowest order. Note that the time scale of Hasselmann's kinetic equation is proportional to ε^{-4} , where ε is a small wave-steepness.

A different approach designed for treating inhomogeneous wave fields, albeit with narrow spectra, was suggested by Alber (1978) and used by him and others to study the instability of homogeneous wave-field to inhomogeneous disturbances. Alber's findings are actually the stochastic counterpart of the well-known deterministic Benjamin–Feir instability, obtained for the cubic Schrödinger equation. The growth

rates of the inhomogeneous instabilities are proportional to ε^2 , reflecting the fact that the time scale of Alber's equation is proportional to ε^{-2} . Although Alber does not state it specifically, the choice of his initial small inhomogeneous disturbances discloses a certain correlation between their phases and those of the homogeneous base state.

From the cubic Schrödinger equation, it is known that the Benjamin–Feir instability, does not lead to a permanent end state, but to an unsteady series of modulation and demodulation cycles, called the Fermi–Pasta–Ulam recurrence phenomenon (see Stiassnie & Kroszynski 1982).

The study of the stochastic counterpart of the Fermi–Pasta–Ulam recurrence is the main goal of the present article. This goal is obtained by integrating Alber's equation numerically.

The only known attempt to obtain subsequent evolution for the solution of Alber's equation, is that of Janssen (1983). Janssen used an asymptotic method to solve the problem near the threshold of instability and obtained a solution which is characterized by an initial small overshoot followed by an oscillation around its time-asymptotic value. In §6, we show that our numerical calculation recovers Janssen's result, but that the behaviour at genuinely unstable points is profoundly different; for the latter points, the deviations from the initial stage are substantial, and moreover the results are of a recurrent nature.

The linear stability analysis is revisited in §2. The physical interpretation of the inhomogeneous disturbance is discussed in §3. The numerical scheme for long-time computations of Alber's equation is given in §4. The results are reported in §5, and discussed in §6.

2. Linear stability analysis

2.1. Alber's equation

Alber's (1978) equation for narrow-banded random surface waves, on infinitely deep water, and in one spatial dimension reads:

$$i\left(\frac{\partial\rho}{\partial t} + \frac{1}{2}\sqrt{\frac{g}{k_0}}\frac{\partial\rho}{\partial x}\right) - \frac{1}{4}\sqrt{\frac{g}{k_0^3}}\frac{\partial^2\rho}{\partial r\partial x} = \sqrt{gk_0^5}\rho(x, r, t)\left[\rho\left(x + \frac{r}{2}, 0, t\right) - \rho\left(x - \frac{r}{2}, 0, t\right)\right], \quad (2.1)$$

where $\rho(x, r, t)$ is the two-point space correlation function defined as:

$$\rho(x, r, t) = \langle A(x + \frac{1}{2}r, t)A^*(x - \frac{1}{2}r, t) \rangle. \quad (2.2)$$

The angle brackets denote the ensemble average, and the asterisk stands for the complex conjugate.

In (2.2), $A(x, t)$ is the complex envelope of the narrow-banded sea, (around k_0), related to the free-surface elevation $\eta(x, t)$ through

$$2\eta(x, t) = A(x, t)\exp(i(k_0x - \sqrt{gk_0}t)) + *, \quad (2.3)$$

where g is the acceleration due to gravity. In the above equations and elsewhere in this paper, x is the horizontal coordinate and t is the time.

Alber's equation (2.1) is based on the cubic Schrödinger equation, which requires that the bandwidth should be of order εk_0 , where $\varepsilon = O(1)$ is a typical wave slope that will be specified later.

2.2. Correlation function for homogeneous seas

Following Kinsman (1965, p. 377), a homogeneous random ocean surface is given by the stochastic integral:

$$2\eta(x, t) = \exp(i(k_0x - \sqrt{gk_0}t)) \int_{-\infty}^{\infty} \exp(i[(k - k_0)x - (\sqrt{gk} - \sqrt{gk_0})t + \theta(k)]) \times \sqrt{S(k)} dk + *, \quad (2.4)$$

where $\theta(k)$ is a random phase with uniform distribution in $(-\pi, \pi]$, and $S(k)$ is the energy-spectrum.

From (2.3) and (2.4),

$$A(x, t) = \int_{-\infty}^{\infty} \exp(i[(k - k_0)x - (\sqrt{gk} - \sqrt{gk_0})t + \theta(k)]) \sqrt{S(k)} dk. \quad (2.5)$$

Substituting (2.5) into (2.2) gives

$$\begin{aligned} \rho(x, r, t) = & \int_{-\infty}^{\infty} \int_{-\infty}^{\infty} \left\langle \exp \left(i \left[(k_1 - k_0) \left(x + \frac{r}{2} \right) - (\sqrt{gk_1} - \sqrt{gk_0})t + \theta_1(k_1) \right] \right) \right. \\ & \cdot \exp \left(-i \left[(k_2 - k_0) \left(x - \frac{r}{2} \right) - (\sqrt{gk_2} - \sqrt{gk_0})t + \theta_2(k_2) \right] \right) \Bigg\rangle \\ & \times \sqrt{S(k_1)S(k_2)} dk_1 dk_2. \end{aligned} \quad (2.6)$$

The only terms that remain after the averaging are those for which $k_2 = k_1$,

$$\begin{aligned} \rho(x, r, t) = & \int_{-\infty}^{\infty} \exp \left(i \left[(k_1 - k_0) \left(x + \frac{r}{2} \right) \right. \right. \\ & \left. \left. - (k_1 - k_0) \left(x - \frac{r}{2} \right) - (\sqrt{gk_1} - \sqrt{gk_0})t + (\sqrt{gk_1} - \sqrt{gk_0})t \right] \right) \\ & S(k_1) dk_1 = \int_{-\infty}^{\infty} \exp(i(k - k_0)r) S(k) dk \equiv \rho_h(r). \end{aligned} \quad (2.7)$$

Thus, the correlation function for a homogeneous sea ρ_h , is independent of x , and is a trivial solution of (2.1).

2.3. Instability of inhomogeneous disturbances

Considering a solution

$$\rho(x, r, t) = \rho_h(r) + \delta\rho_1(x, r, t), \quad (2.8)$$

where δ is the dimensionless inhomogeneity parameter and $\rho_1(x, r, t)$ is an inhomogeneous disturbance. Here, we assume $\delta = o(1)$.

Substituting (2.8) into (2.1) and neglecting terms of order δ^2 ,

$$\begin{aligned} i \left(\frac{\partial \rho_1}{\partial t} + \frac{1}{2} \sqrt{\frac{g}{k_0}} \frac{\partial \rho_1}{\partial x} \right) - \frac{1}{4} \sqrt{\frac{g}{k_0^3}} \frac{\partial^2 \rho_1}{\partial x \partial r} \\ = \sqrt{gk_0^3} \rho_h(r) \left[\rho_1 \left(x + \frac{r}{2}, 0, t \right) - \rho_1 \left(x - \frac{r}{2}, 0, t \right) \right]. \end{aligned} \quad (2.9)$$

Assuming a disturbance of the form

$$\rho_1(x, r, t) = R(r) \left\{ \exp \left(i \left[K \left(x - \frac{1}{2} \sqrt{\frac{g}{k_0}} t \right) - \Omega t \right] \right) + * \right\}, \quad (2.10)$$

where $R(0)$ is real, K is the wavenumber of the disturbance and Ω is its frequency. Note that to obtain instability, $\text{Im}\{\Omega\}$ must be positive.

Substituting (2.10) into (2.9) gives an ordinary differential equation for $R(r)$,

$$\frac{dR}{dr} + \gamma R = G(r), \tag{2.11}$$

where

$$\gamma = 4i\sqrt{\frac{k_0^3}{g} \frac{\Omega}{K}}, \quad G(r) = \frac{4ik_0^4}{K} \rho_h(r) R(0) [\exp(iKr/2) - \exp(-iKr/2)]. \tag{2.12a, b}$$

Assuming that $R(\infty) = 0$, the solution of (2.11) is

$$R(r) = \frac{4ik_0^4}{K} R(0) \exp(-\gamma r) \int_{\infty}^r \rho_h(r') [\exp(ikr'/2) - \exp(-ikr'/2)] \exp(\gamma r') dr'. \tag{2.13}$$

Taking $r = 0$ in (2.13) gives

$$1 = \frac{4ik_0^4}{K} \int_{\infty}^0 \rho_h(r') [\exp(ikr'/2) - \exp(-ikr'/2)] \exp(\gamma r') dr'. \tag{2.14}$$

Substituting (2.7) into (2.14) yields

$$1 = \frac{4ik_0^4}{K} \int_{-\infty}^{\infty} \int_{\infty}^0 \exp(i(k - k_0)r') [\exp(ikr'/2) - \exp(-ikr'/2)] \exp(\gamma r') S(k) dr' dk. \tag{2.15}$$

Integrating (2.15) over r' , noting that $\text{Re}\{\gamma\} < 0$, gives

$$1 = \frac{4ik_0^4}{K} \int_{-\infty}^{\infty} \left\{ \frac{1}{i(k - k_0) + iK/2 + \gamma} - \frac{1}{i(k - k_0) - iK/2 + \gamma} \right\} S(k) dk, \tag{2.16}$$

or

$$1 = 4k_0^4 \int_{-\infty}^{\infty} \frac{S(k) dk}{[i(k - k_0) + \gamma]^2 + K^2/4}, \tag{2.17}$$

which is the final result of this section. For given K and $S(k)$, (2.17) serves to calculate Ω (see 2.12(a)), and to determine conditions for instability and the actual growth rates.

2.4. Three narrow spectra

Any further progress requires us to specify $S(k)$. In our calculation, we have chosen the following three spectra.

(i) *A square spectrum*

$$S = s_0 \quad \text{for} \quad k_0 - W < k < k_0 + W, \tag{2.18}$$

where W is the spectral width.

(ii) *A Lorentz spectrum*

$$S = \frac{0.09 s_0}{[(k - k_0)/W]^2 + 0.02}. \tag{2.19}$$

(iii) *A Gaussian spectrum*

$$S = 1.45 s_0 \exp(-1.64[(k - k_0)/W]^2). \tag{2.20}$$

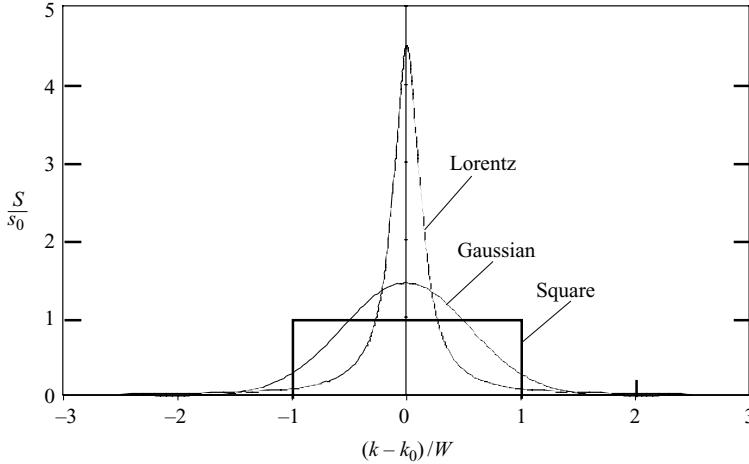


FIGURE 1. Three narrow spectra.

The spectra (ii) and (iii) were normalized to fulfil the following constraints:

$$\int_{-\infty}^{\infty} S(k) dk = 2 W s_0, \quad \int_{k_0-0.9W}^{k_0+0.9W} S(k) dk = 1.8 W s_0. \tag{2.21a, b}$$

Equation (2.21a) guarantees that all spectra have the same total energy, and (2.21b) ensures that they have a comparable width. The three spectra are plotted in figure 1.

2.5. Growth-rate for the square spectrum

Substituting (2.18) into (2.17) and integrating over k :

$$1 = \frac{8k_0^4 s_0}{iK} \left\{ \arctan \left[\frac{2}{K}(\gamma + iW) \right] - \arctan \left[\frac{2}{K}(\gamma - iW) \right] \right\}, \tag{2.22}$$

which can be reduced to

$$\gamma^2 = \frac{K^2}{4} \left[\frac{4W}{K} \coth \left(\frac{K}{8s_0 k_0^4} \right) - 1 \right] - W^2. \tag{2.23}$$

The right-hand side of (2.23) is real. A necessary condition for instability is $\text{Re}\{\gamma\} < 0$, so that $\text{Im}\{\gamma\}$ and $\text{Re}\{\Omega\}$ must vanish. Applying (2.12a), the growth rate is found to be

$$\Omega_I \equiv \text{Im}\{\Omega\} = \frac{K}{4} \sqrt{\frac{g}{k_0^3} \left\{ \frac{K^2}{4} \left[\frac{4W}{K} \coth \left(\frac{K}{8s_0 k_0^4} \right) - 1 \right] - W^2 \right\}}. \tag{2.24}$$

Defining the small steepness parameter

$$\varepsilon = \sqrt{4s_0 W} k_0 = o(1), \tag{2.25}$$

and the non-dimensional variables

$$\tilde{\Omega}_I = \Omega_I / \varepsilon^2 \sqrt{gk_0}, \quad \tilde{K} = K / \varepsilon k_0, \quad \tilde{W} = W / \varepsilon k_0; \tag{2.26a-c}$$

(2.24) is rewritten as:

$$\tilde{\Omega}_I = \frac{\tilde{K}}{4} \sqrt{\tilde{K} \tilde{W} \coth(\tilde{K} \tilde{W} / 2) - \tilde{K}^2 / 4 - \tilde{W}^2}. \tag{2.27}$$

2.6. Growth rate for the Lorentz and Gaussian spectra

Starting from (2.19) and following a similar procedure to that outlined in the previous section, we obtain for a Lorenz spectrum

$$\tilde{\Omega}_l = \frac{\tilde{K}}{4} \left(\sqrt{2 - \tilde{K}^2/4} - 0.1425\tilde{W} \right). \quad (2.28)$$

The result for the Gaussian spectrum, (2.20), can only be given in an implicit form:

$$0.11 \tilde{W} \tilde{K} = \text{Im} \left\{ \mathbf{W} \left(\frac{0.64 \tilde{K}}{\tilde{W}} + \frac{5.14 i \tilde{\Omega}_l}{\tilde{W} \tilde{K}} \right) \right\}. \quad (2.29)$$

The function $\mathbf{W}(z)$ of the complex variable z , is defined in Abramowitz & Stegun (1972, eq. (7.1.3), p. 297); it is related to the complementary error function through

$$\mathbf{W}(z) = e^{-z^2} \text{erfc}(-iz). \quad (2.30)$$

2.7. Results of linear-stability analysis

The non-dimensional growth rate $\tilde{\Omega}_l$, see (2.26a), for the three different spectra is shown in figure 2.

Figure 2 gives nine solid isolines for each spectrum, for which $\tilde{\Omega}_l = 0.05, 0.1, 0.15, \dots, 0.45$. The broken lines represent the marginal stability cases, i.e. $\tilde{\Omega}_l = 0$. Note that $\tilde{\Omega}_l = 0$ also on $\tilde{K} = 0$. For all three spectra, the values of $\tilde{\Omega}_l$ at $\tilde{W} = 0$, i.e. for non-random waves, are identical and reach a maximum $\tilde{\Omega}_l = 0.5$ at $\tilde{K} = 2$, and have $\tilde{\Omega}_l = 0$ at $\tilde{K} = 2\sqrt{2}$. For the Lorentz and Gaussian spectra, the regions of instability are bounded, whereas that of the square spectrum extends to infinity, albeit with ever decreasing growth rates, along the line $\tilde{W} = 0.5 \tilde{K}$. This singular behaviour is attributed to the abrupt structure of the square spectrum. Despite the very different structure of the square and Gaussian spectra, the isolines $\tilde{\Omega}_l = 0.45, 0.40, 0.35$ are surprisingly similar (see figure 3). This similarity becomes even more profound when compared to behaviour of the same isolines for the Lorentz spectrum, also given in figure 3. Note that the case of vanishing spectral width, i.e. $W = 0$, corresponds to the deterministic problem, for which the well-known Benjamin–Feir instability is recovered.

3. Interpretation of the initial disturbance

3.1. Spectral interpretation of the initial conditions

In (2.10), the decay rate $R(r)$ is introduced, and there are no limitations on R except that $R(0)$ is real and $R(\infty) = 0$. In this section, the spectral interpretation of the inhomogeneous disturbance will be derived.

The influence of the small initial disturbance on the homogeneous spectrum can be found by dividing the spectrum in a similar way to (2.8):

$$S(x, k) = S_h(k) + \delta S_1(x, k). \quad (3.1)$$

To find an interpretation for S_1 we start with (2.6); by replacing $S(k)$ with $S(k, x)$, we obtain:

$$\rho(x, r, t) = \int_{-\infty}^{\infty} \exp(i(k - k_0)r) \sqrt{S(k, x + \frac{1}{2}r, t) S(k, x - \frac{1}{2}r, t)} dk. \quad (3.2)$$

Note that (3.2) falls into line with equations (46)–(49) of Crawford, Saffman & Yuen (1980).

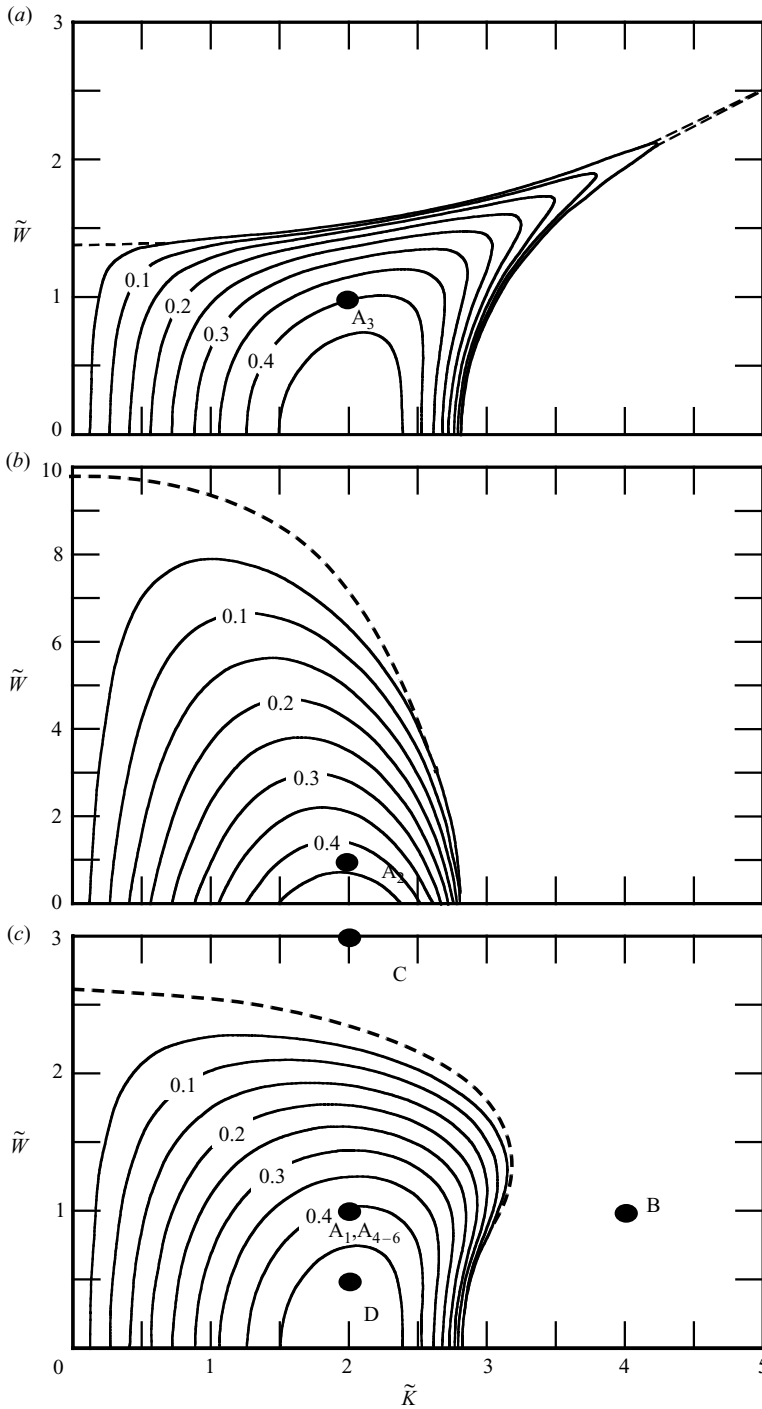


FIGURE 2. Isolines of the non-dimensional growth-rate $\tilde{\Omega}_l$ for three spectra: (a) square spectrum; (b) Lorentz spectrum; (c) Gaussian spectrum. Dots refer to the cases for which long-time evolution is studied.

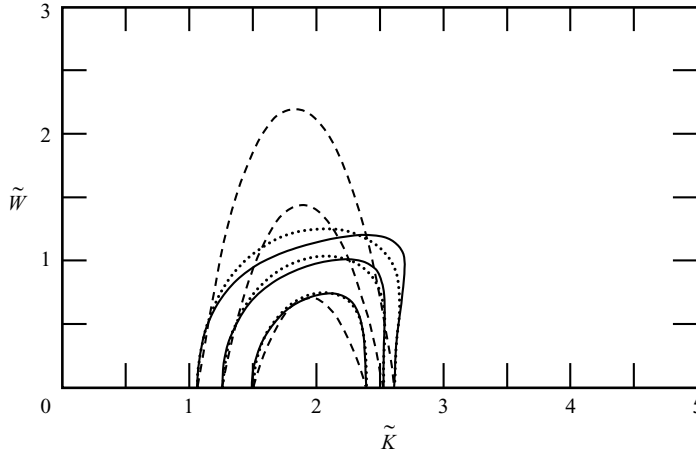


FIGURE 3. Three isolines of the growth rate $\tilde{\Omega}_I = 0.35, 0.40, 0.45$, for three different spectra: (a) —, square spectrum; (b) ---, Lorentz spectra; (c) ···, Gaussian spectra.

Using (3.1) and approximating the value under the square root in (3.2) up to order δ :

$$\sqrt{S(k, x + \frac{1}{2}r, t) S(k, x - \frac{1}{2}r, t)} = S_h(k, t) + \frac{1}{2}\delta [S_1(k, x + \frac{1}{2}r, t) + S_1(k, x - \frac{1}{2}r, t)] + o(\delta^2). \tag{3.3}$$

Substituting (3.3) into (3.2)

$$\rho(x, r, t) = \int_{-\infty}^{\infty} \exp(i(k - k_0)r) \{S_h(k, t) + \frac{1}{2}\delta [S_1(k, x + \frac{1}{2}r, t) + S_1(k, x - \frac{1}{2}r, t)]\} dk. \tag{3.4}$$

Equation (2.10) at $t = 0$ gives,

$$\rho_1(x, r) = 2R(r) \cos(Kx). \tag{3.5}$$

Similarly, for the spectral disturbance at $t = 0$, we assume,

$$S_1(x, k) = 2s(k) \cos(Kx). \tag{3.6}$$

Substituting (3.6) into (3.4) using (3.5) and (2.7),

$$2R(r) = \int_{-\infty}^{\infty} s(k) [\exp(i(k - k_0 + K/2)r) + \exp(i(k - k_0 - K/2)r)] dk. \tag{3.7}$$

Taking the r to χ Fourier transform of (3.7),

$$2 \int_{-\infty}^{\infty} R(r) \exp(-i\chi r) dr = \int_{-\infty}^{\infty} \int_{-\infty}^{\infty} s(k) [\exp(i(k - k_0 + K/2 - \chi)r) + \exp(i(k - k_0 - K/2 - \chi)r)] dr dk. \tag{3.8}$$

Integrating the right-hand side over r :

$$\begin{aligned} \frac{1}{\pi} \int_{-\infty}^{\infty} R(r) \exp(-i\chi r) dr &= \int_{-\infty}^{\infty} s(k) [\delta(k - k_0 + \frac{1}{2}K - \chi) + \delta(k - k_0 - \frac{1}{2}K - \chi)] dk \\ &= s(k_0 + \chi - \frac{1}{2}K) + s(k_0 + \chi + \frac{1}{2}K). \end{aligned} \tag{3.9}$$

Neglecting terms of order K^2 , give an equation for $s(k)$:

$$s(k) = \frac{1}{2\pi} \int_{-\infty}^{\infty} R(r) \exp(-i(k - k_0)r) dr. \tag{3.10}$$

Equations (3.1), (3.6) and (3.10) give the initial spectrum.

Note the similarities between the pair $(\rho_h(r), S_h(k))$ and the pair $(R(r), s(k))$ as demonstrated by their interrelations:

$$\rho_h(r) = \int_{-\infty}^{\infty} S_h(k) \exp(i(k - k_0)r) dk, \tag{3.11a}$$

$$S_h(k) = \frac{1}{2\pi} \int_{-\infty}^{\infty} \rho_h(r) \exp(-i(k - k_0)r) dr, \tag{3.11b}$$

$$R(r) = \int_{-\infty}^{\infty} s(k) \exp(i(k - k_0)r) dk, \tag{3.12a}$$

$$s(k) = \frac{1}{2\pi} \int_{-\infty}^{\infty} R(r) \exp(-i(k - k_0)r) dr, \tag{3.12b}$$

3.2. Connection to the initial surface elevation η

To calculate the initial surface elevation η , we start from (2.4), (3.1) and (3.6) at $t = 0$:

$$\begin{aligned} 2\eta(x) &= \int_{-\infty}^{\infty} \exp(i[kx + \theta(k)]) \sqrt{S(k, x)} dk + * \\ &= \int_{-\infty}^{\infty} \exp(i[kx + \theta(k)]) \sqrt{S_h(k) + 2\delta s(k) \cos(Kx)} dk + *. \end{aligned} \tag{3.13}$$

To first order in δ , (3.13) can be written:

$$2\eta = \left[\int_{-\infty}^{\infty} \exp(i(kx + \theta(k))) \sqrt{S_h} dk + \cos(Kx) \int_{-\infty}^{\infty} \exp(i[kx + \theta(k)]) \sqrt{\frac{\delta^2 s^2}{S_h}} dk \right] + *, \tag{3.14}$$

which shows that the phase $\theta(k)$, of the inhomogeneous disturbance is not free, and is related to the phase of the homogeneous spectrum.

Equation (3.14) can also be written as:

$$\begin{aligned} 2\eta = \int_{-\infty}^{\infty} \left\{ \exp(i(kx + \theta(k))) \sqrt{S_h(k)} + \frac{1}{2} \exp(i((k + K)x + \theta(k))) \sqrt{\frac{\delta^2 s^2(k)}{S_h(k)}} \right. \\ \left. + \frac{1}{2} \exp(i((k - K)x + \theta(k))) \sqrt{\frac{\delta^2 s^2(k)}{S_h(k)}} \right\} \sqrt{dk} + *. \end{aligned} \tag{3.15}$$

A shift of the integration variables in the last two terms on the right-hand side gives:

$$\begin{aligned} 2\eta = \int_{-\infty}^{\infty} \left\{ \exp(i(kx + \theta(k))) \sqrt{S_h(k)} + \frac{1}{2} \exp(i(kx + \theta(k - K))) \sqrt{\frac{\delta^2 s^2(k - K)}{S_h(k - K)}} \right. \\ \left. + \frac{1}{2} \exp(i(kx + \theta(k + K))) \sqrt{\frac{\delta^2 s^2(k + K)}{S_h(k + K)}} \right\} \sqrt{dk} + *. \end{aligned} \tag{3.16}$$

From (3.16), we can see that the phases of the right and left disturbances are identical to those of the homogeneous spectrum, which are random, see also figure 4.

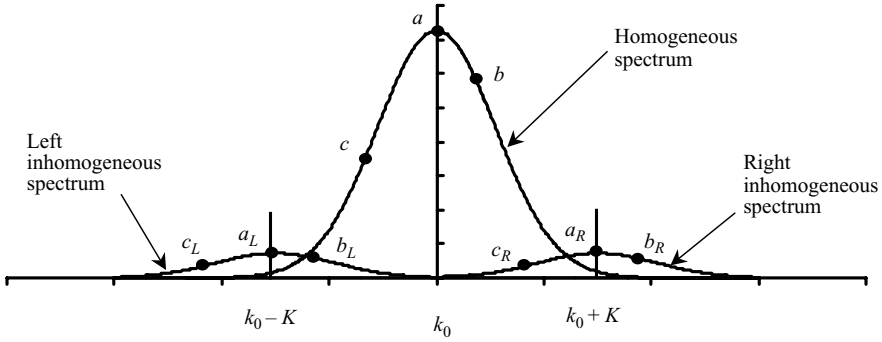


FIGURE 4. Schematic description of the main homogeneous spectrum and the inhomogeneous disturbance (here $S_h(k)$ and $s(k)$ are both Gaussian). As an example, the phases at (a_R, b_R, c_R) and at (a_L, b_L, c_L) are the same as at (a, b, c) , respectively.

4. Numerical solution of Alber's equation

4.1. Numerical scheme

Albers equation (2.1), rewritten in terms of the following non-dimensional and stretched variables:

$$\tilde{\rho} = \frac{k_0^2}{\varepsilon^2} \rho, \tilde{\xi} = \varepsilon k_0 \left(x - \frac{1}{2} \sqrt{\frac{g}{k_0}} t \right), \tilde{\tau} = (\varepsilon^2 \sqrt{gk_0}) t, \tilde{r} = \varepsilon k_0 r,$$

reads:

$$i \frac{\partial \tilde{\rho}}{\partial \tilde{\tau}} + 2\lambda \frac{\partial^2 \tilde{\rho}}{\partial \tilde{\xi} \partial \tilde{r}} - 2\nu \tilde{\rho} [\tilde{\rho}(\tilde{\xi} + \frac{1}{2}\tilde{r}, 0) - \tilde{\rho}(\tilde{\xi} - \frac{1}{2}\tilde{r}, 0)] = 0, \tag{4.1}$$

where, $\nu = 1/2$ and $\lambda = -1/8$.

Formulating (4.1) as a finite-difference scheme, approximating the time derivative by a forward difference, and the $\tilde{\xi}$ and \tilde{r} derivatives by central differences:

$$i \left(\frac{\tilde{\rho}_{(n,j,\ell+1)} - \tilde{\rho}_{(n,j,\ell)}}{\Delta \tilde{\tau}} \right) + \frac{2\lambda}{4\Delta \tilde{\xi} \Delta \tilde{r}} (\tilde{\rho}_{(n+1,j+1,\ell)} - \tilde{\rho}_{(n-1,j+1,\ell)} - (\tilde{\rho}_{(n+1,j-1,\ell)} - \tilde{\rho}_{(n-1,j-1,\ell)})) - 2\nu \tilde{\rho}_{(n,j,\ell)} [\tilde{\rho}_{(n+j\Delta\tilde{r}/(2\Delta\tilde{\xi}),0,\ell)} - \tilde{\rho}_{(n-j\Delta\tilde{r}/(2\Delta\tilde{\xi}),0,\ell)}] = 0, \tag{4.2}$$

where the index n represents points along the $\tilde{\xi}$ axis, $\tilde{\xi} = n\Delta\tilde{\xi}$, $n = 0, 1, 2, \dots, N$; and $N + 1$ is the number of points along this axis. The subscript j represents points along the \tilde{r} axis, where $\tilde{r} = j\Delta\tilde{r}$, $j = 0, 1, 2, \dots, M$; and $M + 1$ is the number of points along the \tilde{r} axis. ℓ represents time steps where $\tilde{\tau} = \ell\Delta\tilde{\tau}$, $\ell = 0, 1, 2, \dots$.

A schematic description of the domain is shown in figure 5.

The numerical time-stepping scheme is formulated as follows:

$$\tilde{\rho}_{(n,j,\ell+1)} = \tilde{\rho}_{(n,j,\ell)} + \frac{i\lambda\Delta\tilde{\tau}}{2\Delta\tilde{\xi}\Delta\tilde{r}} (\tilde{\rho}_{(n+1,j+1,\ell)} - \tilde{\rho}_{(n-1,j+1,\ell)} - (\tilde{\rho}_{(n+1,j-1,\ell)} - \tilde{\rho}_{(n-1,j-1,\ell)})) - 2i\Delta\tilde{\tau}\nu\tilde{\rho}_{(n,j,\ell)} [\tilde{\rho}_{(n+j\Delta\tilde{r}/(2\Delta\tilde{\xi}),0,\ell)} - \tilde{\rho}_{(n-j\Delta\tilde{r}/(2\Delta\tilde{\xi}),0,\ell)}]. \tag{4.3}$$

After several attempts, the following values were taken for the differential steps: $\Delta\tilde{\xi} = \pi/100$, $\Delta\tilde{r} = \pi/40$, and $\Delta\tilde{\tau} = 2.5 \times 10^{-5}$. Taking smaller values did not have a significant effect.

4.2. Periodicity in $\tilde{\xi}$

We restrict ourselves to periodic solutions in $\tilde{\xi}$ so that on the boundary $\tilde{\xi} = \tilde{\xi}_{end}$, $\tilde{\rho}_{(N,j,\ell)} = \tilde{\rho}_{(0,j,\ell)}$.

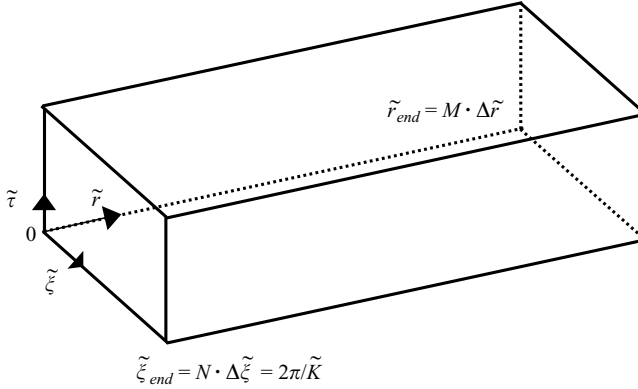


FIGURE 5. Schematic description of the numerical domain.

The last term on the right-hand side of (4.3) depends on values of $\tilde{\rho}$ at $\tilde{\xi} = (n\Delta\tilde{\xi} + j\Delta\tilde{\tau}/2)$ which can be larger than $\tilde{\xi}_{end} = N\Delta\tilde{\xi}$. Again, the periodicity condition is used: $\tilde{\rho}(\tilde{\xi} + 2p\pi, \tilde{r}, \tilde{\tau}) = \tilde{\rho}(\tilde{\xi}, \tilde{r}, \tilde{\tau})$, where $p = 1, 2, \dots$, or $\tilde{\rho}_{(n+pN, j, \ell)} = \tilde{\rho}_{(n, j, \ell)}$.

The values of $\tilde{\rho}$ along $\tilde{r} = 0$, depend on points outside the domain $0 \leq \tilde{r} \leq \tilde{r}_{end}$. Specifically, the second term on the right-hand side of (4.3) depends on $\tilde{\rho}_{(n, -1, \ell)}$. From the definition of $\tilde{\rho}$, (2.2), we see that $\tilde{\rho}(\tilde{\xi}, -\tilde{r}, \tilde{\tau}) = \tilde{\rho}^*(\tilde{\xi}, \tilde{r}, \tilde{\tau})$, so we can calculate the value of $\tilde{\rho}$ along $\tilde{r} = 0$, from the condition: $\tilde{\rho}_{(n, -1, \ell)} = \tilde{\rho}_{(n, 1, \ell)}^*$.

4.3. Condition at large \tilde{r}

Theoretically, the \tilde{r} axis extends to infinity, however for practical reasons, the axis must be truncated. After several attempts, the following analysis led to the boundary condition that was used for large \tilde{r} . We start with (3.2), approximating $S(k, x)$ by a square spectrum in $(k - k_0) \in (-w, w)$, and integrating, leads to:

$$\rho(x, r, t) = 2\sqrt{S(x + \frac{1}{2}r, t)S(x - \frac{1}{2}r, t)} \frac{\sin(wr)}{r}. \tag{4.4}$$

For $r = 0$: $\rho(x, 0, t) = 2S(x, t)w$, thus $S(x, t) = \rho(x, 0, t)/2w$; substituting back into (4.4), and switching to dimensionless quantities:

$$\tilde{\rho}(\tilde{\xi}, \tilde{r}, \tilde{\tau}) = \sqrt{\tilde{\rho}(\tilde{\xi} + \frac{1}{2}\tilde{r}, 0, \tilde{\tau})\tilde{\rho}(\tilde{\xi} - \frac{1}{2}\tilde{r}, 0, \tilde{\tau})} \frac{\sin(\tilde{w}\tilde{r})}{\tilde{w}\tilde{r}}, \tag{4.5}$$

which is the boundary condition used at large \tilde{r} .

The influence of the extent of the \tilde{r} domain was checked for several values: $\tilde{r}_{end} = 10\tilde{\xi}_{end}$, $30\tilde{\xi}_{end}$ and $50\tilde{\xi}_{end}$. The effect of this closure is shown in figure 6, where the maximum value of $\tilde{\rho}(\tilde{r} = 0)$ is presented as a function of the non-dimensional time, $\tilde{\tau}$. It can be seen that all three lines are indistinguishable up to $\tilde{\tau} = 17.5$, (more than 300 wave periods); whereas the lines for the two larger domains overlap throughout the computation. The value of $\Delta\tilde{\tau}$ is kept constant in all cases, so the value of M is 400, 1200 and 2000, according to the increasing size of the domain.

For the case $\tilde{r}_{end} = 30\tilde{\xi}_{end}$ and $\tilde{r}_{end} = 50\tilde{\xi}_{end}$, the value $\tilde{\rho}_{max}(\tilde{r} = 0)$ remained at $\tilde{\xi} = 0$, $\tilde{\xi}_{end}$ throughout the computation (i.e. for $\tilde{\tau} < 35$). This was also the case for $\tilde{r}_{end} = 10\tilde{\xi}_{end}$, but only for $\tilde{\tau} < 17.5$. Since there was no difference between $\tilde{r}_{end} = 30\tilde{\xi}_{end}$ and $\tilde{r}_{end} = 50\tilde{\xi}_{end}$, all the simulations presented in the sequel are with $\tilde{r}_{end} = 30\tilde{\xi}_{end}$.

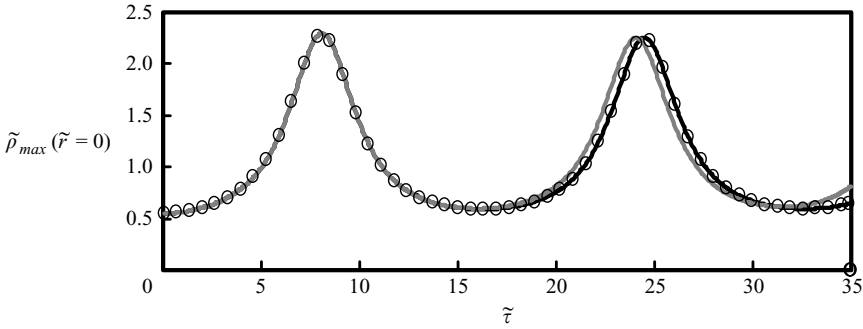


FIGURE 6. The influence of the extent of the \tilde{r} domain on the maximum value of $\tilde{\rho}$ at $\tilde{r}=0$ as a function of non-dimensional time $\tilde{\tau}$, for: —, $\tilde{r}_{end} = 10\tilde{\xi}_{end}$; - - -, $\tilde{r}_{end} = 30\tilde{\xi}_{end}$; \circ , $\tilde{r}_{end} = 50\tilde{\xi}_{end}$. These calculations are for a homogenous Gaussian spectrum and an inhomogeneous Gaussian disturbance with $\tilde{K} = 2$, $\tilde{W} = 1$, $\delta = 0.1$.

4.4. Invariants of motion

In Janssen (1983), we find that the solution to our problem satisfies certain conservation laws, and he continues to specify the first three of them. The same invariants are mentioned in Janssen (2003). Note that the existence of more than three invariants could serve as an indicator to the integrability of Alber’s equation. The first invariant which relates to the total energy is:

$$I_1 = \int_0^{2\pi/K} \rho(x, 0, t) dx. \tag{4.6}$$

The relative deviation of I_1 at all times from its value at $t=0$ did not exceeded 10^{-7} throughout the calculations.

The second invariant which depends on values along r is:

$$I_2 = \int_0^{2\pi/K} \int_{-\infty}^{\infty} \kappa S' dx d\kappa, \tag{4.7}$$

where:

$$S'(x, \kappa, t) = \int_{-\infty}^{\infty} \rho(x, r, t) e^{i\kappa r} dr. \tag{4.8}$$

Since $\rho(t=0)$ is real and symmetric in r ; $I_2(t=0)=0$. Thus, we cannot compare the values of I_2 at all times to the initial value. However, an additional justification for using $\tilde{r}_{end} = 30\tilde{\xi}_{end}$, rather than $\tilde{r}_{end} = 10\tilde{\xi}_{end}$ or $\tilde{r}_{end} = 50\tilde{\xi}_{end}$, can be achieved by comparing I_2 for $\tilde{r}_{end} = 10\tilde{\xi}_{end}$, $\tilde{r}_{end} = 30\tilde{\xi}_{end}$, and $\tilde{r}_{end} = 50\tilde{\xi}_{end}$. Figure 7 shows the value of I_2 (in logarithmic scale) as a function of dimensionless time $\tilde{\tau}$. It can be seen that the values of I_2 for the $\tilde{r}_{end} = 30\tilde{\xi}_{end}$ case are three orders of magnitude smaller then the ones for $\tilde{r}_{end} = 10\tilde{\xi}_{end}$, and overlap the one for $\tilde{r}_{end} = 50\tilde{\xi}_{end}$.

The third invariant which depends both on the values along $r=0$, through its first term, and the values along the r axis, through its second term, is:

$$I_3 = \int_0^{2\pi/K} \rho^2(x, 0, t) dx - \frac{1}{4} \int_0^{2\pi/K} \int_{-\infty}^{\infty} \kappa^2 S' dx d\kappa. \tag{4.9}$$

The relative deviation of I_3 at all times from its value at $t=0$ did not exceeded 2% throughout all calculated evolutions.

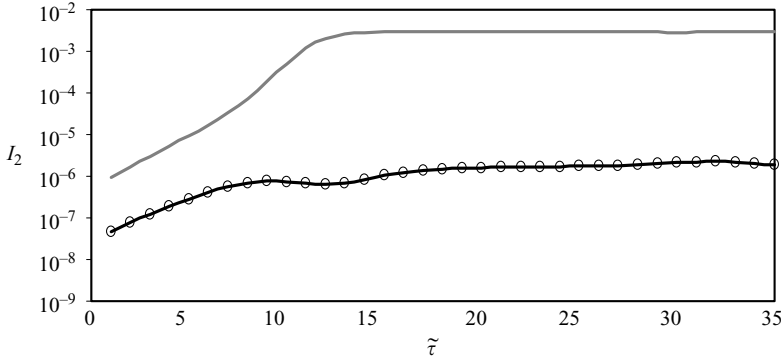


FIGURE 7. The influence of the extent of the r domain on the invariant I_2 as a function of the non-dimensional time $\tilde{\tau}$, for: —, $\tilde{r}_{end} = 10\tilde{\xi}_{end}$; - - -, $\tilde{r} = 30\tilde{\xi}_{end}$; \circ , $\tilde{r} = 50\tilde{\xi}_{end}$. Same case as figure 6.

5. Results of the numerical simulations

5.1. Description of the initial conditions

In order to apply the numerical scheme given in the previous section, the initial value of $\tilde{\rho}$ must be given. These initial conditions are set by (2.8) and by (2.10). It can be seen that there are several degrees of freedom. For example, the initial homogeneous distribution of $\tilde{\rho}_h$ depends only on the initial spectrum (3.11a), which can be a square spectrum (2.18), a Lorentz spectrum (2.19), or a Gaussian spectrum (2.20). For these spectra we obtain, respectively:

$$\tilde{\rho}_h(\tilde{r}, \tilde{\tau} = 0) = \frac{\sin(\tilde{W}\tilde{r})}{2\tilde{W}\tilde{r}}, \tag{5.1}$$

$$\tilde{\rho}_h(\tilde{r}, \tilde{\tau} = 0) = \frac{0.9\pi}{4\sqrt{2}} \exp(-0.1\tilde{r}\tilde{W}\sqrt{2}), \tag{5.2}$$

$$\tilde{\rho}_h(\tilde{r}, \tilde{\tau} = 0) = \frac{1.133\sqrt{\pi}}{4} \exp(-((\tilde{r}\tilde{W})^2/6.45)). \tag{5.3}$$

These correlation functions depend on one free parameter \tilde{W} .

From (2.10), we can see that the value of the inhomogeneous disturbance wave number \tilde{K} , and the inhomogeneity parameter δ are also free quantities. The decay rate $\tilde{R}(\tilde{r})$ that appears in (2.8) is also free; however one could choose the initial inhomogeneous spectral disturbance, and then use (3.12a) to calculate $\tilde{R}(\tilde{r})$.

The influence of various initial conditions will be discussed in this section. The different cases studied are summarized in table 1 and marked by dots in figures 2, 15 and 16.

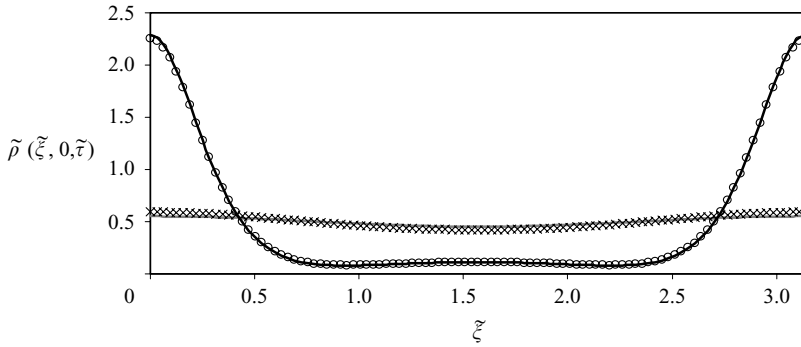
5.2. Reference case (A_1)

The chosen reference case is unstable, its initial homogenous and inhomogeneous spectra are Gaussian with $\tilde{W} = 1.0$, $\tilde{K} = 2.0$, and the small inhomogeneous parameter $\delta = 0.1$.

In figure 8, the value of $\tilde{\rho}(\tilde{\xi}, \tilde{r} = 0)$, which is a representative of the energy distribution, is presented at four different times, $\tilde{\tau} = 0, 8.25, 16.25, 24.5$; which, as can be seen from figure 6, correspond to the initial value, the first peak, the next lowest point, and the next peak, respectively. As we can see from figure 8, the distribution of the energy changes from a nearly even distribution at $\tilde{\tau} = 0$, to the

Case	δ	\tilde{K}	\tilde{W}	$\tilde{\Omega}_1$	Initial homogeneous spectrum S_h	Inhomogeneous disturbance spectrum s	See figure
A ₁	0.1	2.0	1.0	0.405	Gaussian	Gaussian	2
A ₂	0.1	2.0	1.0	0.425	Lorentz	Lorentz	2
A ₃	0.1	2.0	1.0	0.4	Square	Square	2
A ₄	0.1	2.0	1.0	0.405	Gaussian	Square Width = 0.1 \tilde{W}	2
A ₅	1	2.0	1.0	0.405	Gaussian	Square Width = 0.1 \tilde{W}	2
A ₆	10	2.0	1.0	0.405	Gaussian	Square Width = 0.01 \tilde{W}	2
B	0.1	4.0	1.0	0	Gaussian	Gaussian	2
C	0.1	2.0	2.0	0	Gaussian	Gaussian	2
D	0.1	2.0	0.5	0.47	Gaussian	Gaussian	2
E ₁	0.1	1.0	0.5	0.31	Gaussian	Square Width = 0.1 \tilde{W}	16
E ₂	0.1	1.4	0.5	0.406	Gaussian	Square Width = 0.1 \tilde{W}	16
P ₁	0.1	2.0	7.017	0 ⁺	Lorentz	Square Width = 0.1 \tilde{W}	15
P ₂	0.1	2.0	7.5	0	Lorentz	Square Width = 0.1 \tilde{W}	15
P ₃	0.1	2.0	6.5	0.074	Lorentz	Square Width = 0.1 \tilde{W}	15

TABLE 1. Summary of parameters chosen for the various simulations.

FIGURE 8. The value of $\tilde{\rho}$ as a function of $\tilde{\xi}$, at $\tilde{r} = 0$ for different times: —, $\tilde{\tau} = 0$; —, $\tilde{\tau} = 8.25$; \times , $\tilde{\tau} = 16.25$; \circ , $\tilde{\tau} = 24.5$. case A₁.

case where most of the energy is concentrated at the two ends of the region at $\tilde{\tau} = 8.25$, and back to (almost) the initial distribution of $\tilde{\rho}$ at $\tilde{\tau} = 16.25$ (for $\tilde{\tau} = 24.5$, the picture returns to that of $\tilde{\tau} = 8.25$). In figure 9(a), the real part of $\tilde{\rho}$ as a function of \tilde{r} at $\tilde{\xi} = \tilde{\xi}_{end}/2$, is plotted as a function of $\tilde{r}/\tilde{\xi}_{end}$ for the same times as appear in figure 8. It can be seen that the values of the real part of $\tilde{\rho}$ are nearly identical for $\tilde{\tau} = 0$, $\tilde{\tau} = 16.25$, and also the values at $\tilde{\tau} = 8.25$ and $\tilde{\tau} = 24.5$ are the same. In figure 9(b), the imaginary part of $\tilde{\rho}$ at the same cross-section is plotted, recurrence is less evident. Note that the magnitude of the real part is ten thousand times larger than the magnitude of the imaginary part.

5.3. The influence of the initial linear growth rate on the long-time evolution

In figure 10, the long-time evolution of $\tilde{\rho}(0, 0, \tilde{\tau})/\tilde{\rho}_h(0)$ is presented for the cases A₁, B, C, D (see figure 2c). In all of these cases, the starting homogeneous, and the inhomogeneous disturbance spectra were Gaussian, and the inhomogeneity parameter δ , was 0.1. Two of the cases (D, A₁) are in the unstable region, whereas the other two cases (C, B) are in the stable region. The initial value is 1.1 in all cases. In all cases, the value of $\tilde{\rho}(0, 0, \tilde{\tau})$ (the maximum value at $\tilde{r} = 0$) does not go below the initial

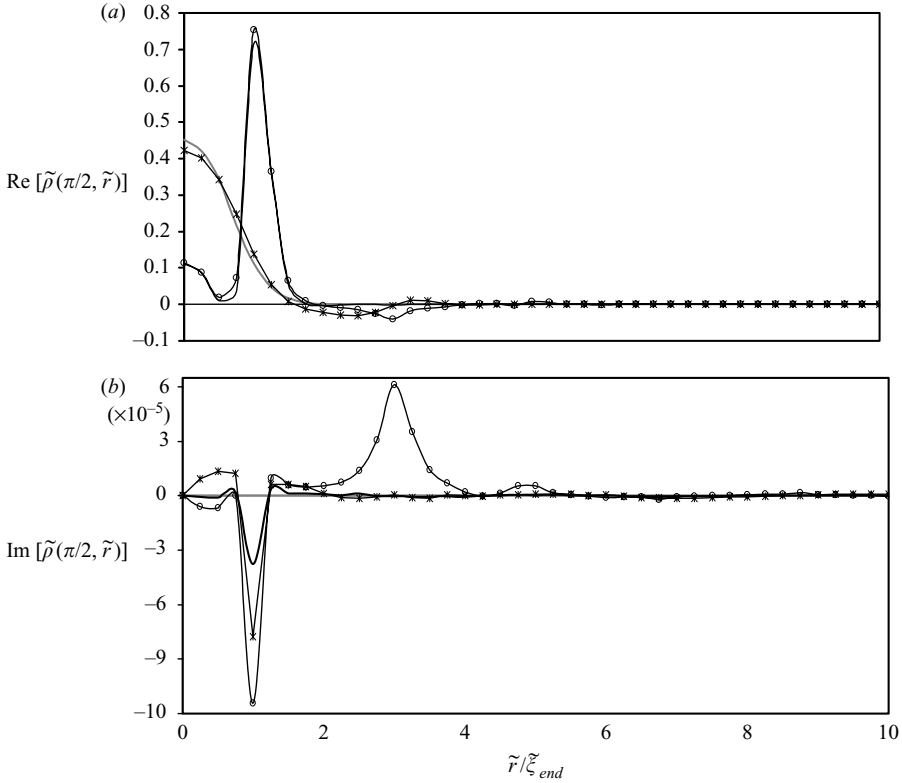


FIGURE 9. The values of (a) the real part of $\tilde{\rho}$ and (b) the imaginary part as a function of $\tilde{\tau}/\tilde{\xi}_{end}$, at the cross-section $\tilde{\xi} = \tilde{\xi}_{end}/2$, for different times. —, $\tilde{\tau} = 0$; —, $\tilde{\tau} = 8.25$; *, $\tilde{\tau} = 16.25$; ○, $\tilde{\tau} = 24.5$. case A_1 .

homogeneous value. It can be clearly seen from figure 10 that the value of $\tilde{\rho}(0, 0, \tilde{\tau})$ increases to 5.8 times the initial homogenous value for case D, which is the most unstable case treated here, with a growth rate of 0.47. In case A_1 , which is unstable and its growth rate is 0.405, this value increases to 4.5 times the initial value. For the third and fourth cases that appear in figure 10, the corresponding points in figure 2c are in the stable region. Case C which has the same \tilde{K} as case A_1 , but \tilde{W} is 3 times larger, initially increases to 1.25 of the initial homogeneous value, and oscillates with decreasing value to the initial homogeneous value. The fourth case, B, in which the spectrum has the same \tilde{W} as case A_1 , but the wavenumber of the disturbance \tilde{K} is doubled, decreases monotonically to the initial homogeneous value.

5.4. Influence of the shape of the initial spectrum

Figure 11 illustrates the long-time evolution of $\tilde{\rho}(0, 0, \tilde{\tau})/\tilde{\rho}_h(0)$ for the three different initial homogenous spectra $S_h(k)$, described in §2, when the small inhomogeneous disturbance spectrum $s(k)$ has the same structure as the homogeneous one, and the inhomogeneity parameter is $\delta = 0.1$. These cases are marked as A_1 , A_2 , and A_3 in figure 2. Figure 11 demonstrates the difference between the Gaussian spectrum, the square spectrum and the Lorentz spectrum. As we can see, the maximal value of $\tilde{\rho}$ for the Lorentz profile is greater than those for the square spectrum and for the Gaussian spectrum.

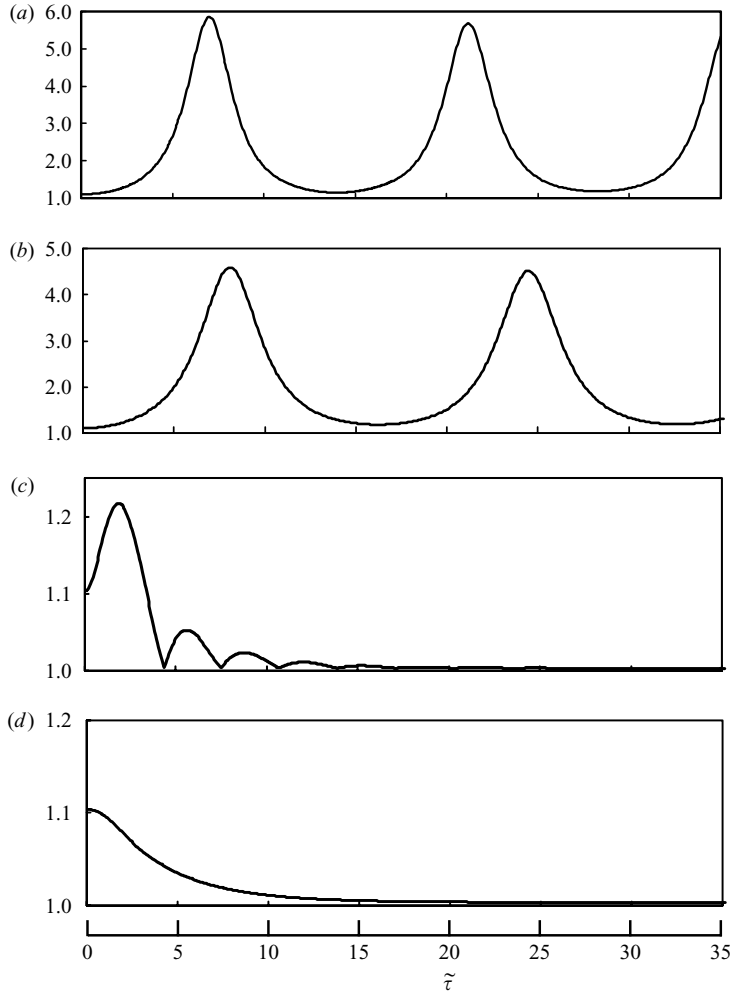


FIGURE 10. The value of $\tilde{\rho}(0, 0, \tilde{\tau})/\tilde{\rho}_h(0)$ as a function of time, for four different initial growth rates, cases (a) D, (b) A_1 , (c) C and (d) B of figure 2(c) and table 1.

We can see from table 1 that indeed its growth rate is also greater, for the same initial \tilde{W} and \tilde{K} . Besides the maximal value, the differences are relatively small, and in particular, the period of the recurrence for the three spectra is similar.

5.5. Influence of the shape of the inhomogeneous disturbance

The influence of the shape of the inhomogeneous disturbance is checked for four different cases.

(i) The reference case with Gaussian homogenous and inhomogeneous disturbance spectra (case A_1).

(ii) Gaussian homogenous spectrum with a small square inhomogeneous disturbance, $\delta = 0.1$, and the width of the spectrum $s(k)$ is 10% of the width of $S_h(k)$, as shown schematically in figure 12 (case A_4).

(iii) Case A_5 in which the width of the inhomogeneous disturbance spectrum is the same as in case A_4 , but $\delta = 1.0$.

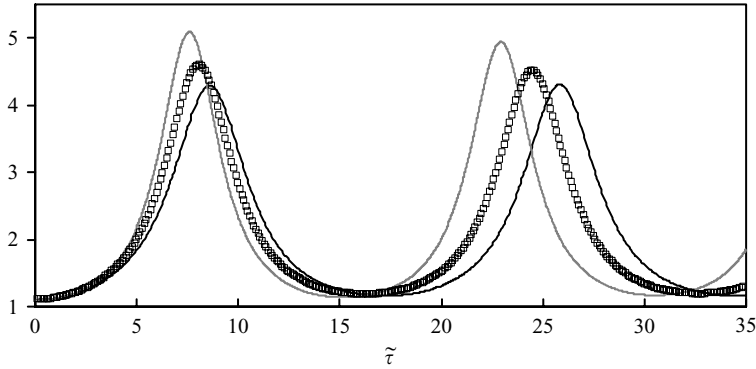


FIGURE 11. The values of $\tilde{\rho}(0, 0, \tilde{\tau})/\tilde{\rho}_h(0)$ as a function of time for three different initial spectra: —, square (A_1); □, Gaussian (A_3); ···, Lorentz (A_2).

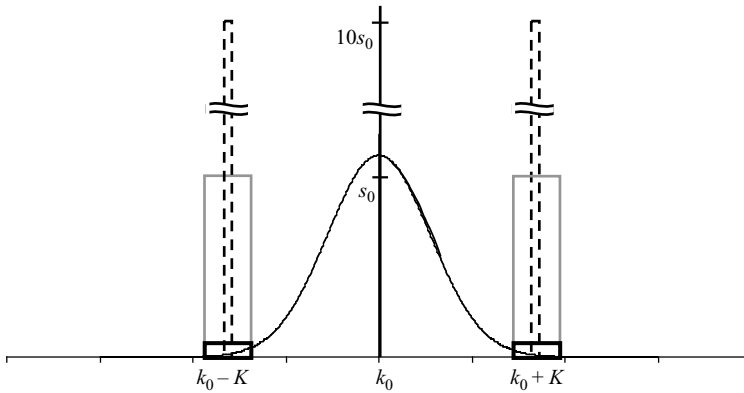


FIGURE 12. Schematic description of the initial homogenous spectrum and the inhomogeneous disturbances, —, case A_4 ; —, case A_5 ; - - -, case A_6 .

(iv) Case A_6 for which the width of the disturbance is $0.01\tilde{W}$ but $\delta = 10$, so that the total area under the disturbance spectra is the same as in case A_5 .

In figure 13, the value of $\tilde{\rho}(0, 0, \tilde{\tau})/\tilde{\rho}_h(0)$ is shown. It can be seen that although the inhomogeneous disturbance is different from case to case the maximum value of $\tilde{\rho}(0, 0, \tilde{\tau})/\tilde{\rho}_h(0)$ is the same, and seems to depend only on the initial homogeneous width \tilde{W} , and the disturbance wavenumber \tilde{K} . However, owing to the weak disturbance in case A_4 the period of recurrence is much larger, as was shown by Stiassnie & Kroszynski (1982) for the deterministic problem. Despite the difference in the disturbance width between cases A_5 and A_6 , the values of $\tilde{\rho}(0, 0, \tilde{\tau})/\tilde{\rho}_h(0)$ are nearly identical, probably because the energy of the disturbance is the same in both cases.

6. Discussion

Alber (1978) formulated an equation which is appropriate for the study of random inhomogeneous wave fields with narrow spectra. This equation, now known as Alber's equation, enabled him to discover the stochastic parallel to the Benjamin–Feir instability. In this paper, we have shown by numerical computations that a stochastic parallel to the Fermi–Pasta–Ulam recurrence also exists.

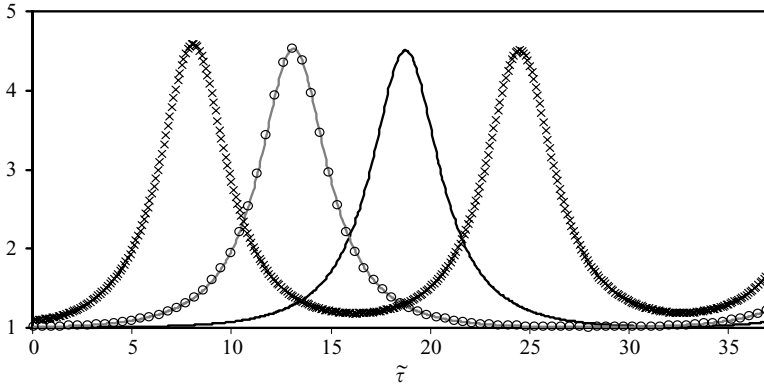


FIGURE 13. The values of $\tilde{\rho}(0, 0, \tilde{\tau})/\tilde{\rho}_h(0)$ as a function of time, for four different initial inhomogeneous disturbance spectra: \times , Case A₁; —, Case A₄; - - -, Case A₅; \circ , Case A₆.

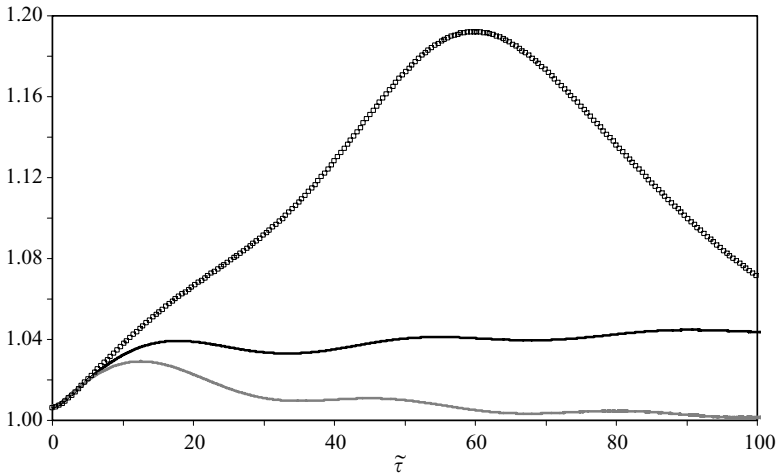


FIGURE 14. The value of $\tilde{\rho}(0, 0, \tilde{\tau})/\tilde{\rho}_h(0)$ as a function of time for three cases near the threshold of instability. —, P₁; - - -, P₂; $\square \square$, P₃.

As mentioned in §1, the only known attempt to obtain subsequent evolution for the solution of Alber’s equation, is that of Janssen (1983). Janssen used an asymptotic method to solve the problem near the threshold of instability and obtained a solution which is characterized by an initial small overshoot followed by an oscillation around its time-asymptotic value. In figure 14 we present results of the behaviour of our numerical solution near and at the threshold of instability for the case of an initial Lorentz spectrum with a small square disturbance, for $\tilde{K} = 2.0$ and $\tilde{W} = 6.5, 7.017$ and 7.5 . These three cases are marked in figure 15 as P₃, P₁ and P₂, respectively. The results in figure 14 for the cases P₁ and the P₂ are similar to what one would expect from Janssen’s description of his asymptotic approximation. Note that the result for P₃ is recurring with a rather long recurrence-period (the period is approaching infinity as we approach the marginal stability line from below).

Note that the numerical recurrence demonstrated by our results finds some support in Janssen (1983). He defines $W(x, p, t)$, (given by the r to p Fourier-transform of $\rho(x, r, t)$) and obtains a transport equation for W , (his equation (11)). He observed that

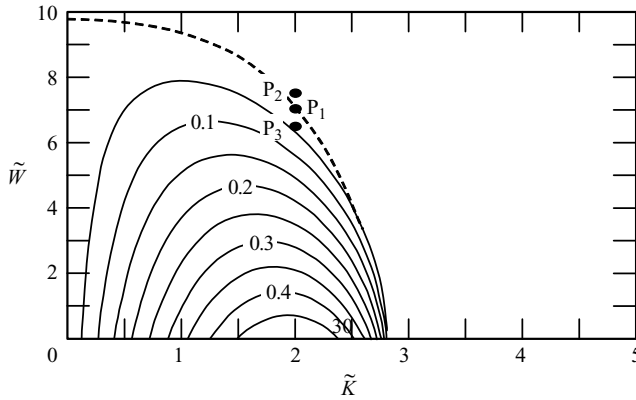


FIGURE 15. Three cases near the marginal-stability curve, see table 1.

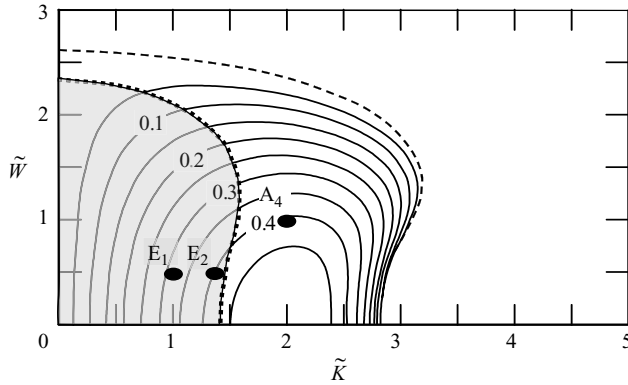


FIGURE 16. The distinction between cases of simple and complex recurrence.

this transport equation turns out to be invariant under the transformation $t \rightarrow -t$, $p \rightarrow -p$, indicating, in our opinion, that the energy transfer (owing to the spatial inhomogeneities) is possibly reversible. However, it turns out that the above condition is probably necessary, but not always sufficient. To demonstrate this we have chosen cases for which $2\tilde{K}$ are also within the unstable region, see points E_1 and E_2 in figure 16. This property is shared by all points within the shaded zone in figure 16. From figure 17, we can see that the graphs for cases E_1 , E_2 are very different from that of A_4 , they are not recurring. The growth rate of A_4 is equal to that of E_2 which is larger than that of E_1 ; however, the value of $\tilde{\rho}_{max}$ is larger for E_2 than for A_4 , and largest for E_1 . ($\tilde{\rho}_{max}$ is the maximum value that $\tilde{\rho}(\tilde{\xi}, 0, \tilde{\tau})$ obtains for a fixed $\tilde{\tau}$, and $\tilde{\xi} \in (0, \tilde{\xi}_{end})$, for complex recurrence the maximum value is moving and does not stay at $\tilde{\xi} = 0$ any more.) This could be explained from the values of the growth rates of $2\tilde{K}$ disturbances, which are 0.48, 0.23 and 0 for cases E_1 , E_2 and A_4 , respectively. We call this type of behaviour ‘complex recurrence’, adopting the terminology of Yuen & Ferguson (1978) who have obtained analogous results for the Schrödinger equation.

We must stress that in the present study the initial disturbance spectra are profoundly inhomogeneous, through their phase relation to the homogenous spectrum, in contrast to previous studies for which all initial phases were independent and randomly chosen.

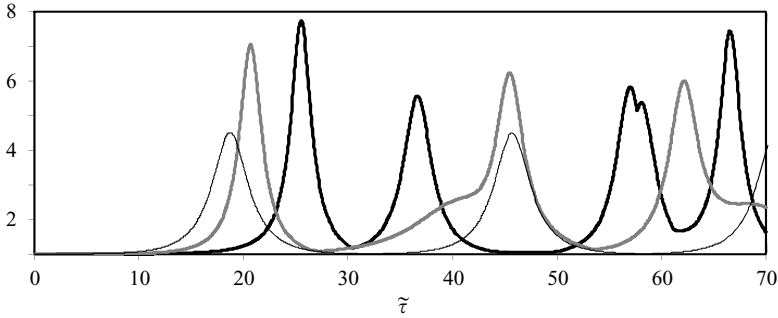


FIGURE 17. The value of $\tilde{\rho}_{max}/\tilde{\rho}_h(0)$ as a function of time for two cases in the complex recurrence zone, E_1 and E_2 , and a case in the simple recurrence zone A_4 , see table 1. —, E_1 ; —, E_2 ; —, A_4 .

The question about the possible manifestation of such inhomogeneous disturbances in nature is crucial for the physical feasibility, not only of the newly calculated evolutions, but also for Alber’s (1978) linear stability analysis.

One possible mechanism to generate such disturbances is related to sea-swell interaction, for which the coexistence of a narrow-banded random sea and of a monochromatic swell of much larger wavelength, is assumed.

The superharmonics and subharmonics which are generated by their interaction (which are rather close to free waves), can probably serve as the inhomogeneous disturbances, very similar in nature to those described in § 3.

Janssen (2003) applied a Monte Carlo approach to a naive discretization of Zakhaov’s equation, using random initial phases, and obtained an irreversible widening of the spectrum. Similar results were also found by Dysthe *et al.* (2003) who have used the modified Schrödinger equation with random initial phases. It seems plausible that recurrence could be recovered by their approaches, provided that appropriate initial phase-relations are used. The overall averaged spectrum calculated from our computations resembles the irreversible Monte Carlo results. This overall spectrum is

$$\bar{\bar{S}}(k) = \frac{1}{T} \int_0^T \bar{S}(k, t) dt, \tag{6.1}$$

where T denotes the recurrence time, and $\bar{S}(k, t)$ is the space-averaged spectrum:

$$\bar{S}(k, t) = \frac{K}{2\pi} \int_0^{2\pi/K} S(k, x, t) dx. \tag{6.2}$$

$S(k, x, t)$ in (6.2) is inspired by (47) to (50) of Crawford *et al.* (1980), and given by

$$S(k, x, t) = \frac{1}{2\pi} \int_{-\infty}^{\infty} \rho(x, r, t) \exp(-i(k - k_0)r) dr. \tag{6.3}$$

In figure 18(a) we give $\bar{\bar{S}}(k)/S_h(0)$ and compare it to $S_h(k)/S_h(0)$ for the case A_1 .

In figure 18(b) we show $\bar{S}(k, t)/S_h(0)$ at $t = 0, t = T/4, t = T/2$. The curve at $T = T/2$ demonstrates an almost equal partition of the energy between the base spectrum and the disturbances. The area under the graph of $\bar{\bar{S}}(k)/S_h(0)$ in figure 18(a) is 0.6% larger than that under $\bar{S}(k, t)/S_h(0)$ at $t = 0$.

Alber’s original equation is not restricted to unidirectional cases, and we believe that similar results to ours will be found for two-dimensional narrow spectra, in the

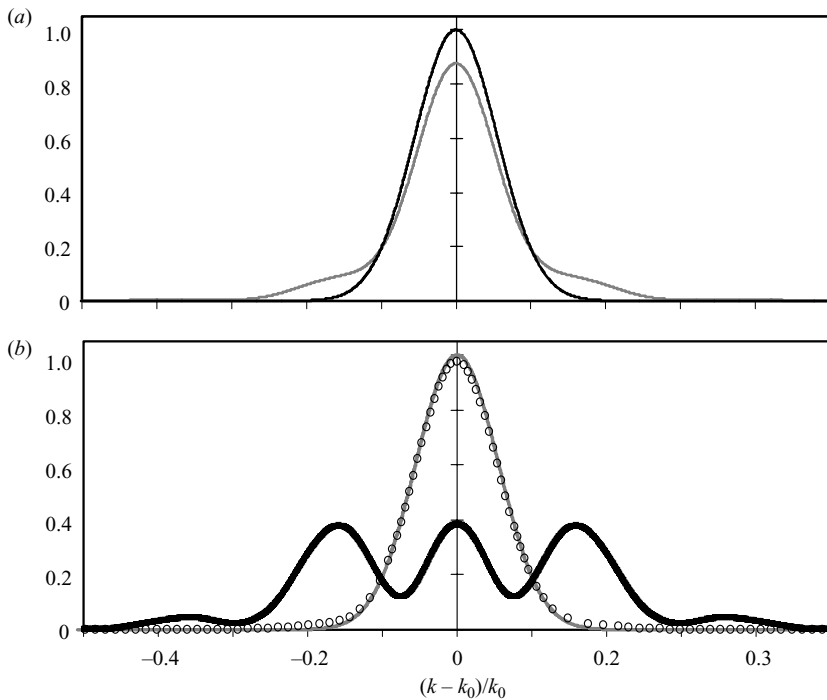


FIGURE 18. (a) The overall averaged spectrum $\text{---}, \bar{\bar{S}}(k)/S_h(0)$; compared to $\text{---}, S_h(k)/S_h(0)$. (b) The spatial averaged spectra $\text{---}, \bar{S}(k, t)/S_h(0)$ for $t=0$; $\circ\circ$, $t=T/4$; --- , $t=T/2$.

future. The extension to broad spectra is a much more complicated issue, and it still awaits the development of an appropriate model equation. In this respect, we should mention preliminary attempts to study sea-states governed by a system, of two Alber's equations, such as in Stiassnie (2001) and Shukla, Markland & Stenflo (2006).

Note that the time scales involved in the recurrence are much shorter than those of the kinetic equation. We can say that the choice of overall random phases in the derivation of the kinetic equation, which results in longer time-scales also 'average out' the recurrence phenomenon. The kinetic equation is the main tool for calculating nonlinear interaction in wave-forecasting models, see Komen *et al.* (1994), and it will probably remain so for some time to come. However, model equations, such as Alber's equation can be helpful when addressing phenomena governed by smaller time/space scales, such as the development of freak waves.

This research was supported by The Israel Science Foundation (Grant 695/04) and by the US–Israel Binational Science Foundation (Grant 2004-205). The authors are grateful to Dr A. Zuevsky for his help in the early stages of this work.

REFERENCES

- ABRAMOWITZ, M. & STEGUN, A. 1972 *Handbook of Mathematical Functions*. Dover.
- ALBER, I. E. 1978 The effects of randomness on the stability of two-dimensional wavetrains. *Proc. R. Soc. Lond. A* **363**, 525–546.
- ANNENKOV, S. Y. & SHRIRA, V. I. 2006 Role of non-resonant interactions in evolution on nonlinear random water wave fields. *J. Fluid Mech.* **561**, 181–207.

- CRAWFORD, D. R., SAFFMAN, P. G. & YUEN, H. C. 1980 Evolution of a random inhomogeneous field of nonlinear deep-water gravity waves. *Wave Motion* **2**, 1–16.
- DYSTHE, K. B., TRULSEN, K., KROGSTAD, H. E. & SOCQUET-JUGLARD, H. 2003 Evolution of a narrow-band spectrum of random surface gravity waves. *J. Fluid Mech.* **478**, 1–10.
- HASSELMANN, K. 1962 On the non-linear energy transfer in a gravity-wave spectrum. Part 1. General theory. *J. Fluid Mech.* **12**, 481–500.
- JANSSEN, P. A. E. M. 1983 Long-time behaviour of a random inhomogeneous field of weekly nonlinear surface gravity waves. *J. Fluid Mech.* **133**, 113–132.
- JANSSEN, P. A. E. M. 2003 Nonlinear four-wave interaction and freak waves. *J. Phys. Oceanogr.* **33**, 863–884.
- KINSMAN, B. 1965 Wind waves, their generation and propagation on the ocean surface. Prentice-Hall.
- KOMEN, G. J., CAVALERI, L., DONELAN, M., HASSELMANN, K., HASSELMANN, S. & JANSSEN, P. A. E. M. 1994 *Dynamics and Modelling of Ocean Waves*. Cambridge University Press.
- SHUKLA, P. K., MARKLAND, M. & STENFLO, L. 2006 Modulational instability of nonlinear interacting incoherent sea states. *Sov. Phys., J. Exp. Theor. Phys. Lett.* **84**, 645–649.
- STIASSNIE, M. 2001 Nonlinear interaction of inhomogeneous random water wave. *ECMWF Report of the Workshop on Ocean Waves Forecasting, Reading, July 2–4*, pp. 39–52.
- STIASSNIE, M. & KROSZYNSKI, U. I. 1982 Long time evolution of an unstable water-wave train. *J. Fluid Mech.* **116**, 207–225.
- YUEN, H. C. & FERGUSON, W. E. 1978 Relationship between Benjamin–Feir instability and recurrence in the nonlinear Schrödinger equation. *Phys. Fluids* **21**, 1275–1278.
- ZAKHAROV, V. E. 1968 Stability of periodic waves of finite amplitude on the surface of a deep fluid. *J. Appl. Mech. Tech. Phys. (Engl. Transl.)* **2**, 190–194.